Multi-group Radiation Diffusion Convergence in Low-density Foam Experiments

K. W. McLean*, S. J. Rose

Centre for Inertial Fusion Studies (CIFS), The Blackett Laboratory, Imperial College, London SW7 2AZ

Abstract

We present an in-depth analysis of a Marshak radiation wave moving through an iron-oxide (Fe_2O_3) foam using a 1D multigroup diffusive radiation transport model, MDART (Multigroup Diffusion Algorithm for Radiation Transport). We consider the consequences of under-resolving the group structure and address how this could lead to incorrect conclusions in the analysis of general supersonic radiation wave experiments. We also provide an analysis of the types of experimental outcome one may incorrectly link to physical effects but are in fact due to poor simulation practice.

Keywords: High Energy Density, Multigroup Radiation Transport, Diffusion, Marshak Wave, Plasma Radiative Opacity

1. Introduction

Over the past two decades, many experiments have been performed to both observe and analyse supersonic radiation wave phenomena in the laboratory ([1] - [4]), particularly through low-density foams which ensures the radiation wave is not ablative and can maintain supersonic speeds [5].

Such experiments have implications for the modelling of laser-hohlraum interactions in indirect-drive Inertial Confinement Fusion (ICF) and, more recently, in modelling radiative opacities in high energy density (HED) regimes [6]. Owing to their supersonic speed, these types of radiation waves provide a more idealised platform for probing theory since the plasma can be considered static. To model such experiments, the role of radiation must be well understood; indeed, in the case of supersonic waves, the evolution of radiation energy density (governed by the radiation transfer equation) coupled to the material heat equation determines the evolution of the entire system.

Generally, to solve radiation transport fully, one can use discrete ordinates or implicit Monte-Carlo (IMC) methods [7] which provide accurate solutions across all regimes of optical depth. However, where the opacity is sufficiently high, the transport is diffusive and can be well modelled using multigroup flux limited diffusion (FLD), a technique which is common in modelling HED plasmas [8] - [16]. We assume this to be the case in the experiment used as a surrogate for this study, which launched a radiation wave through an iron oxide (Fe_2O_3) foam. Importantly, although there is a non-negligible deviation between exact transport behaviour and FLD [17], the results shown in this paper remain relevant to modelling radiation wave experiments.

The experiment used in this study has implications across HED physics and in particular solar modelling, as discussed in [6] and [18]. To ensure that the computational modelling of this experiment, and all radiation wave experiments modelled using FLD, is as accurate as possible, it is necessary to explore all avenues of error, both physical and computational. With this in mind, this work provides an extensive and thorough consideration of potential computational errors which can jeopardise experimental analysis when FLD methods are used, and provide ways to minimise such errors. To do this, computational input parameters are altered in the 1D Multigroup Diffusion Algorithm for Radiation Transport (MDART) - introduced and benchmarked in section 3 - and the resultant experimental diagnostic signature monitored. A further motivation for this work is that, compared with full transport solutions, FLD algorithms run much quicker and use less memory. Therefore FLD may be more suitable for full statistical modelling of supersonic radiation wave experiments, where experi-

*Corresponding Author

Email address: k.mclean17@imperial.ac.uk (K. W. McLean)

mental uncertainties are very important [6] [3] [19], as discussed in section 5. Thus, a deeper understanding of FLD algorithms will aid experimental campaigns that utilise statistical analysis.

2. Theory

The radiative transfer equation (RTE) [20], is given by

$$\frac{1}{c}\frac{\partial I_\nu}{\partial t} + \mathbf{\Omega}\cdot\nabla I_\nu = \rho\kappa_\nu(T_e)[B_\nu - I_\nu] \tag{1}$$

where I_ν is the specific intensity, $\mathbf{\Omega}$ is a unit vector along the direction of radiation propagation and B_ν is the blackbody intensity given by

$$B_\nu = \frac{2h\nu^3}{c^2}\frac{1}{\exp\left\{\frac{h\nu}{k_B T}\right\} - 1} \tag{2}$$

Note that the form of the RTE given in equation 1 assumes that scattering contributions are negligible. This assumption is reasonable at the temperatures considered but can become important at higher temperatures.

Taking the first solid angle moment of equation 1 gives the radiation energy equation (REE), given by

$$\frac{dE_\nu}{dt} + \nabla\cdot\mathbf{F}_\nu = \rho\kappa_\nu(T_e)c[E_\nu^P(T_e) - E_\nu] \tag{3}$$

This equation, together with the material energy equation:

$$\rho c_V\frac{\partial T_e}{\partial t} = \rho\int_0^\infty \kappa_\nu(T_e)c[E_\nu - E_\nu^P(T_e)]d\nu \tag{4}$$

are the two equations underpinning this numerical study. The energy density, E_ν, and flux, $\mathbf{F}_\nu$, are defined by

$$E_\nu = \frac{1}{c}\int_{4\pi} I_\nu d\Omega \tag{5}$$

$$\mathbf{F}_\nu = \int_{4\pi}\mathbf{\Omega}I_\nu d\Omega \tag{6}$$

In addition to this, we note that $E_\nu^P(T_e)$ is the Planckian energy density at the electron temperature, T_e, ρ is the mass density and c_V is the specific heat capacity at constant volume.

To model how the radiation and material energies change as photons and electrons interact, one must solve equation 3 and 4 simultaneously. To obtain a numerical solution, the entire photon frequency (or energy) space is discretised into N groups, with each group containing a subsection of the total energy content, and bounded between two frequencies ν_a and ν_b. In discretising the frequency space, equation 3 is transformed into N discrete equations with each describing how the radiation contained within group g moves through the material. Splitting equations 3 into N frequency groups (equation 4 is strictly defined as frequency-integrated), each equation takes the form

$$\frac{dE_g}{dt} + \nabla\cdot\vec{F}_g = \rho\bar{\kappa}_{P_g}c[E_g^P(T_e) - E_g] \tag{7}$$

where $\bar{\kappa}_{P_g}$ is a Planckian weighted opacity within group g, which is bounded by frequencies a and b, and defined by

$$\kappa_P = \frac{\int_a^b \kappa_\nu B_\nu(T_e)d\nu}{\int_a^b B_\nu(T_e)d\nu} \tag{8}$$

In the diffusion regime, which is discussed in [21] - [23], the flux is related to the energy density via Fick's law [24]

$$\mathbf{F}_\nu = -D_\nu\nabla E_\nu \tag{9}$$

where D_ν is a diffusion coefficient. Generally, D_ν can be artifically altered to ensure that the radiative flux obeys

$$F_\nu \leq cE_\nu \tag{10}$$

which is known as *flux limiting* [25].

In the non-flux limited regime, where one allows radiation to flow at any arbitrary speed, D_ν takes the form

$$D_\nu = \frac{c}{3\kappa_{R_g}} \tag{11}$$

where κ_R is the Rosseland mean opacity [26] and is defined as

$$\kappa_R^{-1} = \frac{\int_a^b \kappa_\nu^{-1}\frac{\partial B_\nu(T_e)}{\partial T}d\nu}{\int_a^b \frac{\partial B_\nu}{\partial T}(T_e)d\nu} \tag{12}$$

In the flux limited regime, here we take D_ν to be

$$D_\nu = \frac{c}{\left[(3\kappa_\nu)^n + (\frac{\nabla E}{E})^n\right]^{\frac{1}{n}}} \tag{13}$$

which is known as the Larsen flux limiter (order n) [27]. Note that there exists two special cases of the Larsen limiter; n = 1, which is known as the *Wilson sum* limiter and n $\rightarrow \infty$, which is known as the *Wilson max* limiter [28]. A Wilson max limiter is used throughout this study unless otherwise stated.

Using equations 7 through 13, we derive the set of N discrete REEs which are solved in this work, given by

$$\frac{dE_g}{dt} - \nabla \cdot D_g \nabla E_g = \rho \bar{\kappa}_g c[E_g^P(T_e) - E_g] \tag{14}$$

Generally, the quantities listed in equation 14 are functions of space, x, and time, t.

Throughout the study, we consider four approximations, listed in table 1.

Simulation Type	Description
1T	N = 1, $T_r = T_e \forall x, t$
3T [29]	N = 1 , $T_r \neq T_e$
14-Group	N = 14 (Low Resolution)
Nominal	N = 293 (High Resolution)

Table 1: Description of simulation types used in this work.

Note that the 3T algorithm is so called due to historical use with three separate ion, electron and radiation temperatures denoted T_i, T_e and T_r, respectively. In this work $T_e \approx T_i$ but the 3T nomenclature is retained for historical continuity.

We also consider the consequences of using *only one* of the weighted opacities defined in 8 and 12, when solving equation 14. It is important to distinguish the physical role each opacity has in the equation.

2.0.1. Rosseland mean

The Rosseland mean opacity (κ_R) governs how radiation *moves* through the material. In the optically thick (high opacity) limit, this is a diffusive process and any local deposition of energy will spread through the material isotropically [22]. The Rosseland mean therefore affects the *transport* of radiation through the material, which is why it is calculated as a harmonic mean - the regions of lowest opacity is where energy transport is maximised.

2.0.2. Planckian mean

The Planckian mean opacity (κ_P) , along with the specific heat capacity (C_V) of the material, determines the extent to which radiative energy deposition results in an increase in T_e. Planckian opacity is a direct weighted average and is enhanced in regions of energy space where a high number of photons are available for absorption and emission. Photon numbers are governed by the Planckian distribution at the local temperature. The weighting functions using in calculations of κ_R and κ_P are assumed to be calculated at the local electron temperature. However, a more rigorous treatment of the 1T and 3T algorithms would involve weighted opacities calculated at the radiation temperature T_r [30].

3. Numerical method

The set of multigroup equations shown in 14 are discretised as follows:

$$\begin{aligned} \frac{E_{gj}^{t+1} - E_{gj}^{t}}{\Delta t} - \frac{1}{(\Delta x)^2}[D_{gj,j+1}E_{gj+1}^{t+1} - \\ (D_{gj,j+1} + D_{gj-1,j})E_{gj}^{t+1} + D_{gj-1,j}E_{gj-1}^{t+1}] \\ = \rho \kappa_{P_{gj}} c[E_g^P(T_j^{t+1}) - E_{gj}^{t+1}] \end{aligned} \tag{15}$$

where the subscripts and superscripts have the following meanings:

- subscript j denotes the position, in 1D, of the grid point in physical space
- subscript g denotes the group, in frequency (or equivalently, photon energy) space
- superscript t and $t+1$ denote the current and forward timesteps respectively
- the quantity $D_{j,j+1}$ defines the diffusion coefficient for the transport of energy from cell j to cell $j+1$, D is assumed to take the form of a Larsen flux limiter.
- The temperature, denoted T, is the electron temperature. Here we assume that $T_e = T_i$, the ion temperature.

Equation 4 is discretised as

$$\rho c_V \frac{T_j^{t+1} - T_j^t}{\Delta t} = \sum_g \Delta \nu \rho \kappa_g (E_g^{t+1} - E_g^P(T_j^{t+1})) \tag{16}$$

To calculate the sum in equation 16 correctly, we take the temperature change between groups to be sufficiently small that we can introduce partial temperature changes within a single timestep. Thus, the temperature will incrementally change as each group deposits energy into a particular region of the spectrum. This is expressed as

$$T^{t+1} - T^t = \sum_g [\tau_{g+1}^{t+1} - \tau_g^{t+1}] \tag{17}$$

$$\tau_N^{t+1} = T^{t+1} \qquad \tau_0^{t+1} = T^t$$

Thus, the conditions for calculating the energy transport in group g are updated after the solution of group

$g-1$, within a single timestep. An approximate expression for $E_g^{P,t+1}(T_e^{t+1})$ is needed in both 15 and 16 because the energy density at the forward temperature is not known. Assuming the change in temperature is small between groups, we expand around the temperature calculated from the previous group solution, τ_g^{t+1}.

$$\begin{aligned} &E_g^P(T_e^{t+1}) \rightarrow E^P(\tau_{g+1}^{t+1}) \\ &\approx E_g^P(\tau_g^{t+1}) + (\tau_{g+1}^{t+1} - \tau_g^{t+1})\frac{\partial E_g^P(T)}{\partial T}|_{T=\tau_g^{t+1}} \end{aligned} \tag{18}$$

$$\begin{aligned} &\rho c_v \frac{\tau_{g+1,j}^{t+1} - \tau_{gj}^{t+1}}{\Delta t} \\ &= c\rho\kappa_{P_{gj}}\left[E_{gj}^{t+1} - E_g^P(\tau_g^{t+1}) - (\tau_{g+1}^{t+1} - \tau_g^{t+1})\frac{\partial E_g^P(T)}{\partial T}|_{T=\tau_g^{t+1}}\right] \end{aligned} \tag{19}$$

This partial temperature approach is one of many approaches used to overcome the fact that the change in material temperature depends on the radiation density across all frequencies, more approaches are described in [31]. In the limit of infinitely small timesteps, the partial temperature approach tends to the most accurate solution. If the deposition of energy is such that the radiation temperature changes by more than 5%, then the algorithm flags this and the timestep is reduced to mitigate errors associated with a large change in plasma conditions between group solutions. Substitution of 18 and 19 into 15 gives

$$\begin{aligned} &\frac{E_{gj}^{t+1} - E_{gj}^t}{\Delta t} - \frac{1}{(\Delta x)^2}[D_{gj,j+1}E_{gj+1}^{t+1} \\ &- (D_{gj,j+1} + D_{gj-1,j})E_{gj}^{t+1} + D_{gj-1,j}E_{gj-1}^{t+1}] \\ &= \beta_{gj}[E_g^P(T_j^t) - E_{gj}^{t+1}] \end{aligned} \tag{20}$$

$$\beta_{gj} = c\kappa_{P_{gj}} - \frac{c^2\rho^2\kappa_{P_{gj}}^2 \frac{\partial E_g^P(T)}{\partial T}|_{T=\tau_g^{t+1}}}{\frac{\rho c_V}{\Delta t} + c\rho\kappa_{P_{gj}}\frac{\partial E_g^P(T)}{\partial T}|_{T=\tau_g^{t+1}}} \tag{21}$$

$$D_{L_{j,j+1}}^{t+1}(n) = \frac{c}{\left[(3\kappa_{R_{j,j+1}})^n + \left(\frac{E_{j+1}^t - E_j^t}{E_{j,j+1}^t \Delta x}\right)^n\right]^{\frac{1}{n}}} \tag{22}$$

where

$$E_{j,j+1}^t = \frac{E_j^t + E_{j+1}^t}{2} \tag{23}$$

and the value of κ_R used in the flux limiter is defined on the cell boundary. To obtain this value, the Rosseland mean is calculated as a cell boundary temperature $T_{j,j+1}$, defined by

$$T_{j,j+1} = (T_j^4 + T_{j+1}^4)^{\frac{1}{4}} \tag{24}$$

The inclusion of a flux limiter makes the diffusion equation non-linear in E, and here the flux limiter lags in time, meaning that any energy terms defined within the limiter are defined at the current timestep, but used in the calculation of the forward timestep, as shown in equations 20 and 22 [31]. This is reasonable if timesteps are small enough that energy densities don't significantly change across one timestep. All results presented have been tested to convergence in timestep to ensure that flux limiter lagging is numerically accurate.

To solve the system of multigroup equations, 20, and the material equation, 19, a tridiagonal system of linear equations must be solved. The form taken by this system is

$$\tilde{T}\hat{a} = \hat{b} \tag{25}$$

where $\tilde{T}$ is a tri-diagonal matrix consisting of elements which describe the transport of energy from cell j into the neighbouring cells; $j+1$ and $j-1$. The vectors $\hat{a}$ and $\hat{b}$ contain the energy density at the forward and current timestep respectively;

$$\begin{aligned} \hat{a} &= [E_{g1}^{n+1}, E_{g2}^{n+1}, \ldots] \\ \hat{b} &= [E_{g1}^n + \Delta E_{m_{g1}}^n, \ldots] \end{aligned} \tag{26}$$

$$\Delta E_{m_{gj}}^n \equiv \beta_{gj}\Delta t E_g^P(T_j) \tag{27}$$

where $\hat{b}$ includes the deposition of radiative energy into group g due to emission at the local electron temperature, T. The extent of coupling between the radiation energy density, material energy density and electron temperature is contained within the parameter β_{gj}. A LUPP algorithm is used to solve this system [32].

3.1. Boundary conditions

To solve the set of equations given by 20, we specify a right hand boundary which radiates freely into the vacuum and a constant incoming flux at the left hand boundary, which has been shown to give an accurate representation of the material temperature behaviour at the interface [33]. To implement these conditions we follow methods used in [34], which are generalisations of formulas given in [21] and [12].

Defining an outward pointing normal vector at the surface (this is applicable to both left and right boundaries) as $\hat{\Omega}$, then the geometric product representing the

inward going specific intensity will satisfy $\hat{\Omega} \cdot \hat{\Omega}_B < 0$. The outward going specific intensity is taken to satisfy the condition [21]

$$\frac{\int_{\hat{\Omega}\cdot\hat{\Omega}_B>0} d\Omega\hat{\Omega} \cdot \hat{\Omega}_B I(\mathbf{\Omega})}{\int_{\hat{\Omega}\cdot\hat{\Omega}_B>0} d\Omega I(\mathbf{\Omega})} \equiv \langle\mu\rangle \tag{28}$$

where I denotes the specific intensity from any external sources. Using equations 5 and 6, we can rewrite 28 as

$$\frac{\hat{\Omega}_B \cdot \vec{F} - \int_{\hat{\Omega}\cdot\hat{\Omega}_B<0} d\Omega\hat{\Omega} \cdot \hat{\Omega}_B I(\mathbf{\Omega})}{cE - \int_{\mathbf{\Omega}\cdot\hat{\Omega}_B<0} d\Omega I(\mathbf{\Omega})} = \langle\mu\rangle \tag{29}$$

In deriving equation 29, the integral limits are altered using the fact that the $\hat{\Omega} \cdot \hat{\Omega}_B > 0$ and $\hat{\Omega} \cdot \hat{\Omega}_B < 0$ must each span half of the solid angle space, 4π. For the left hand boundary, the value of I will take that of the blackbody intensity - originating from the source which is given as temperature T_D, this results in a boundary condition governed by

$$\frac{1}{2}\langle\mu\rangle cE|_L + \frac{1}{2}F_{out_L} = \frac{caT_D^4}{4} \tag{30}$$

where $E|_L$ is the energy density at the left hand boundary. To derive this expression, the incoming flux has been written in terms of temperature, using the relation

$$F_{inc} = \frac{caT_D^4}{4} \tag{31}$$

The right hand side of the material slab is prescribed to radiate freely into the vacuum. Thus, from equation 29 with $I(\mathbf{\Omega}) = 0$, we recover the simple right hand boundary condition as

$$\hat{\Omega}_B \cdot \vec{F}|_R = \langle\mu\rangle cE|_R \tag{32}$$

where $\vec{F}|_R$ and $E|_R$ are the flux and energy density at the right hand boundary. In this work, both boundaries are set to $\langle\mu\rangle = \frac{1}{2}$, known as the Marshak Boundary condition [35]. Generally, the value of $\langle\mu\rangle$ must always satisfy $0 < \langle\mu\rangle < 1$.

4. Benchmarking

We provide separate comparisons with the benchmark problems of Su & Olson [34], where we consider a 3T problem, and Fleck & Cummings [7], which tests the accuracy of the multigroup algorithm in MDART. Each work considers a radiation drive impinging on a semi-infinite slab of material, calculating the spatially

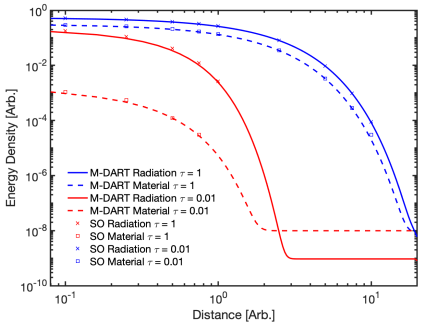

Figure 1: Benchmarking of MDART against Su and Olson single group solution. Results are provided for a selection of normalised timepoints, τ, and for both radiation (blue) and material (red) energy density. For all simulations, $\epsilon = 0.1$.

resolved electron temperature as a function of time. Su & Olson consider the special case of a constant opacity and a specific heat capacity that varies with the cube of temperature, which allows an analytical solution to be obtained. Fleck & Cummings solve the system numerically using an Implicit Monte Carlo algorithm where the opacity varies in both photon frequency and temperature, simulating a more physically realistic scenario.

4.1. Su & Olson

To solve the energy equation analytically, Su & Olson follow work by Pomraning [35] where the material opacity is assumed to be constant and the specific heat capacity is given by

$$C_V = \alpha T^3 \tag{33}$$

where α is an arbitrary proportionality constant. In doing this, equation 14 becomes linear in both E and T_e^4 which, after normalisation, can be solved numerically as discussed in [34]. The authors provide tabulated solutions to two parameters u and v defined as

$$u = \frac{c}{4}\left[\frac{E(x,t)}{F_{inc}}\right] \qquad v = \frac{c}{4}\left[\frac{aT^4(x,t)}{F_{inc}}\right] \tag{34}$$

which, upon appropriate normalisation, are directly comparable to the material and radiation energy densities output from MDART. Two additional parameters are introduced in [34], given by

$$\epsilon = \frac{4a}{\alpha} \qquad \tau = \left(\frac{4ac\kappa}{\alpha}\right)t \tag{35}$$

Figure 1 demonstrates that the 3T (single group) format of MDART shows very good agreement with the analytical solutions from [34].

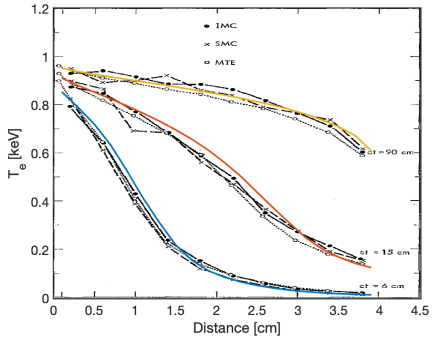

Figure 2: Multigroup simulation of the propagation of a Marshak wave at 3 timepoints for a material with opacity governed by equation 36. Results are compared with the IMC algorithm of [7], who simultaneously compare results for IMC (block dot), Semi Implicit Monte Carlo (SMC), shown as a cross, and the multigroup telegraphers equation (MTE), which is similar to the diffusion approximation. The number of groups used is 60, with groups split linearly in logarithmic space.

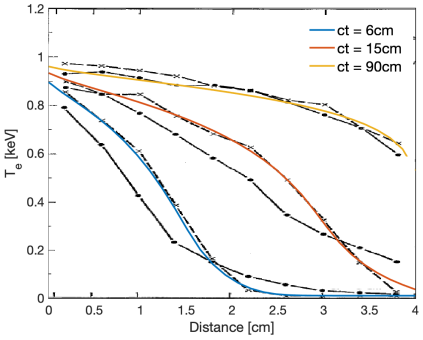

Figure 3: Multigroup simulations of Marshak wave propagation through material with opacity governed by equation 37. Results are to be compared with the dashed line with intermittent crosses, upon which our results are superimposed. The number of groups used in this simulation was 80, with equal spacing in logarithmic space. The full line is related to other changes in the algorithm [7] and is to be ignored for this comparison

4.2. Fleck & Cummings

To test MDART with a more realistic opacity profile, it was also benchmarked against the results of Fleck & Cummings [7], who use an implicit Monte-Carlo scheme to solve the REE with a material opacity profile of the form

$$\kappa(\nu, T) = \frac{F(T)}{\nu^3}\left(1 - \exp\left(-\frac{\nu}{T}\right)\right) \tag{36}$$

Where $F(T)$ is an arbitrary function. This form contains an inverse cubic frequency dependence, representative of a free-free opacity as well as an exponential term accounting for stimulated emission. The first set of solutions provided by Fleck & Cummings are for the simple case of $F(T) = 27$. A comparison between the Implicit Monte Carlo results and the multigroup diffusion method of MDART are shown in figure 2.

We add an additional temperature dependence in the opacity profile, increasing the physical accuracy of the underlying model. To include this, our arbitrary function $F(T)$ now takes the form

$$F(T) = \frac{27}{T^3} \tag{37}$$

A comparison of our results with those of Fleck & Cummings are given in figure 3.

Figures 2 and 3 show good agreement between the multigroup algorithm in MDART and the IMC method used by [7].

5. Radiation wave experiments

When an energetic drive impinges upon a material surface, a radiation wave moves through the foam as the slab is heated to the drive temperature. If the conditions are such that the radiation wavefront travels with a Mach number greater than unity, then the scenario is well modelled using static radiation transport. The position of the Marshak wave, x, as a function of time, t, is determined by [6]:

$$x^2 = A\frac{T^3 t}{\rho^2 c_V \kappa_R} \tag{38}$$

where A is a constant, T is the temperature behind the wavefront, ρ is material density, c_V is specific heat capacity and κ_R denotes the Rosseland mean opacity. Note that the constant, A can be derived exactly, but it is kept as arbitrary for continuity with [6] and owing to the fact that results presented in this paper are concerned only with experimental parameter scaling. From 38, an experiment where the Marshak wave position can be monitored in time is suitable for calculating either the drive temperature, density, specific heat capacity or Rosseland mean opacity - *if the other variables are suitably constrained.*

Sections 6, 7 and 8 detail the computational artefacts which arise when under-resolved FLD algorithms are used to model these types of experiments. The analysis uses the conditions in the Hoarty iron opacity experiment, which is described briefly in section 5.1 and in more detail in [6].

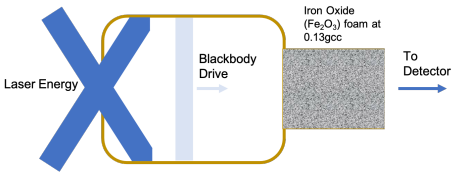

Figure 4: Schematic of experimental set-up. A blackbody drive is produced upon interaction between the laser light and the gold hohlraum walls, and is incident on an Iron-Oxide foam. After traversing the full length of the foam, the wave will breakout, where it detected as an emergent flux [6]. The foam diameter is 2 mm and length 1mm.

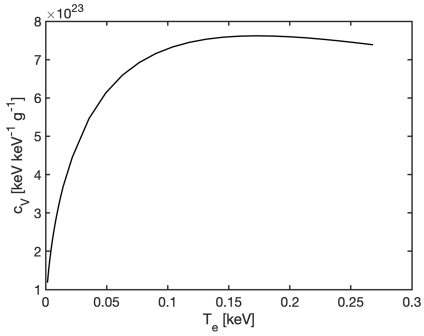

Figure 5: Specific heat capacity used in the simulations. This profile was generated using equation of state tables generated from the Ionised Material Package (IMP) [37].

5.1. Hoarty el al. experiment

This section describes the proposed iron opacity experiment which is a collaboration between the National Ignition Facility (NIF) and Atomic Weapons Establishments (AWE), which is used as a surrogate for this study. In the experiment, radiation wave transit is used to diagnose changes in opacity [6], through monitoring the breakout time, which is the time at which the radiation wave breaks out of foam end. This experiment is aimed to provide an independent test of iron opacities to complement past work which suggest current opacity models are inaccurate [18]. Results from this study will therefore be of considerable interest to the laboratory, plasma and solar physics communities by providing new data on the long running disagreement between opacity measurements and helioseismology in calculating the position of the solar tachocline [36]. The set-up for the Hoarty et al [6] experiment is shown in figure 4.

A hohlraum is irradiated by laser beams at the National Ignition Facility (NIF) which, upon interaction with the gold hohlraum walls, produces an X-ray bath which we take to be Planckian, at temperature $T_D(t)$. This resultant flux is incident on an iron oxide (Fe_2O_3) foam at the far end of the hohlraum. This launches a radiation (Marshak) wave which traverses the full length of the foam before being measured by a DANTE detector. Using MDART, this experiment is modelled assuming a Planckian hohlraum drive at $T_D(t)$. The curved surface of the foam is surrounded by a thin (≈ 25 μm) gold coating which is radially separated from the foam by around 5 μm of vacuum. As the high energy photons penetrate deep into the foam, preceding the main front, this vacuum gap is filled. The energy lost to heating the gold coating does has implications for the Marshak transit time as is discussed in section 9.1. Simulations of this experiment are used to provide temporally and spatially resolved T_e profiles and time resolved emergent flux profiles, the latter of which is directly comparable to the DANTE flux. The experiment simulated consists of a 0.13 g/cc Fe_2O_3 foam of length 1 mm and diameter 2 mm. The specific head capacity used in the simulations is calculated using IMP [37] and is shown in figure 5. The drive profile is assumed be Planckian with an evolution in time given by the red dashed line of figure 4 from [6], which consists of an initial 0.5 ns ramp up to a steady 250 eV drive temperature.

5.2. Experimental analysis

As previously stated, if the radiative opacity is to be probed using this experimental method, it is important to constrain all other physical and experimental parameters as well as possible. Where these parameters are known within error range, it is desirable to perform a full statistical analysis of the experiment which allows one to answer the question; if the signature detected is correct, what is the likelihood that the signal is solely due to a change in opacity?

To perform this type of analysis, Markov Chain Monte Carlo (MCMC) methods can be used [38]. To ensure this method is as efficient as possible, a code is required to be both robust and quick. Flux limited diffusion models are desirable for the latter; they are quicker than discrete ordinates or implicit Monte-Carlo methods - which are closer to 'real transport' solutions. This work is intended to provide an extensive overview of the necessary precautions one must take prior to modelling a radiation wave experiment using FLD. Further, given that Iron is high-Z material, the experiment itself is assumed to be well modelled by diffusive transport. It should be noted that non-negligible deviations exist where wave transit is calculated using FLD or by exact transport [17]. However, it will be shown that the discrepancies identified due to group structure are present regardless of the flux-limiter type used in FLD.

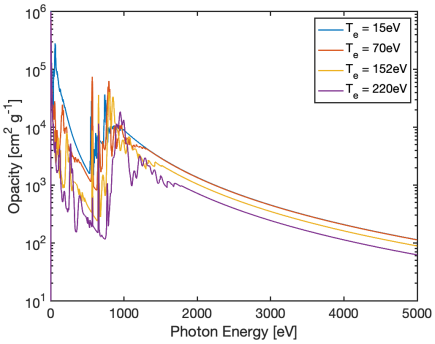

Figure 6: Iron Oxide (Fe_2O_3) radiative opacities calculated using IMP [37] as a function of photon energy at a set of electron temperatures expected to be sampled during the course of the simulation. The K-shell (located at $\approx$ 7 keV) is omitted as it can be neglected in the simulations.

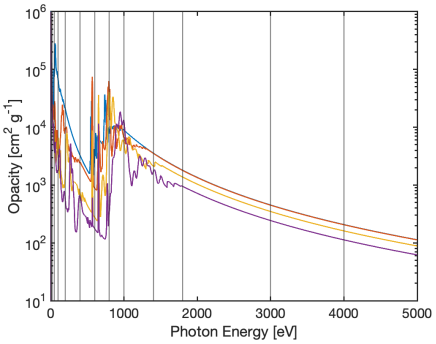

Figure 7: Equivalent of figure 6 with vertical lines representing the boundaries of the underlying 14 group structure. Higher fidelity is applied to low energy regions where many lines are present, with wider groups around the continuum.

6. Convergence simulations: overview

Although the experiment is modelled by Hoarty et al [6] in 2D, the simulations performed in this work are all spatially 1D to allow a more detailed investigation into numerical convergence with a reasonable amount of computational power. The experiment is concerned with breakout time and we expect that 1D will provide sufficient insight into numerical inaccuracies. A brief outline of 2D effects and their expected influence is provided in section 9.1. From here onwards, all simulations have been tested for convergence in timestep and spatial resolution.

6.1. Group structure

The *group structure* used in MDART defines how the energy space is discretised. One must consider how many groups are required and the position of each group, both contribute to solution convergence. In regions where opacity varies highly with photon energy, the group structure should be finer to accommodate this. Inside each defined group, Rosseland and Planckian weighted opacities are still calculated, but are integrated over the group. In the limit that groups are infinitely small ($N \rightarrow \infty$), we recover an opacity spectrum which is fully resolved in frequency, and $\kappa_P \rightarrow \kappa_R$ for each group.

A selection of iron oxide opacities used in this series of simulations is given in figure 6. The spectra used throughout this work are generated using the Ionised Material Package (IMP) [37], a model that assumes ionisation and excitation are in local thermodynamic equilibrium (LTE).

In the simulations, the energy is truncated at 5 keV as testing has shown that the Marshak wave propagation is mainly determined by L-shell interactions. At the temperatures probed in the experiment ($T_e \leq 250$ eV), the number of photons present at K-shell energies ($\approx$ 7 keV) is sufficiently low that they don't affect the problem in any significant way. Including energy groups above 5 keV results in the same solutions as those obtained without. It is clear that where shell structure is present - around 700 eV - 1 keV - the opacity spectrum is complex and a large group number is required here. For the analysis of this section, we provide results for 1T, 3T, 14 group and 293 group algorithms which are described in table 1. The 14 group structure is superimposed over the opacity spectra in figure 7 and shows reasonable detail at low energies with much wider groups around the continuum region of the opacity, where κ_ν varies approximately as ν^{-3}.

An enhanced view of the 293 group structure in provided in figure 8. Note that the group structure is made finer in regions where large opacity changes are present, such as the line at high temperatures centred around 655 eV.

6.2. Tracking the wavefront

Within the simulation, the wavefront can be tracked via electron temperature calculation or through a simulated DANTE flux signature. The latter is comparable with experimental diagnostics but both are included.

6.2.1. Electron temperature

The Marshak wave electron temperature profile, calculated using each algorithm type, is plotted in the top panel of figures 9 - 11. Respectively, these show results as calculated at 1 ns, 1.5 ns and 2 ns.

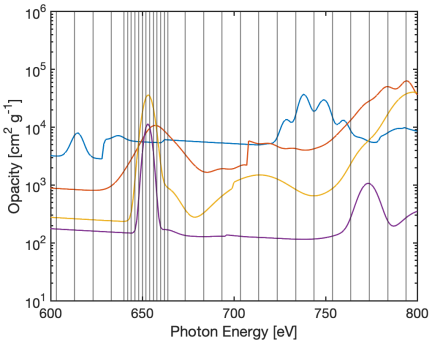

Figure 8: Equivalent of figure 6 with vertical lines representing the boundaries of the underlying 293 group structure. A small energy region of 200 eV is shown to highlight how thin the groups are in this case. Note the even higher fidelity around the main line structures.

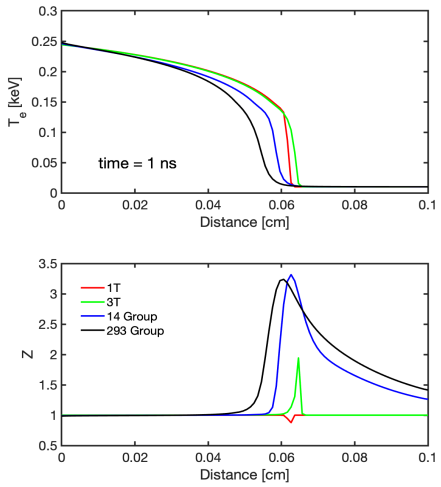

Figure 9: Top: Electron temperature profile across the foam, plotted for each algorithm type and calculated at t = 1 ns. Bottom: Ratio of radiation to electron temperature across foam, calculated at 1 ns.

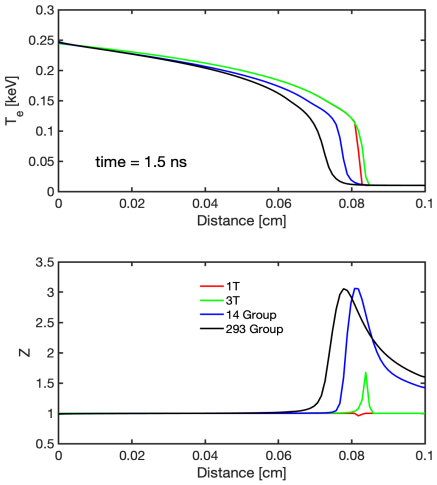

Figure 10: Top: Electron temperature profile across the foam, plotted for each algorithm type and calculated at t = 1.5 ns. Bottom: Ratio of radiation to electron temperature across foam, calculated at 1.5 ns.

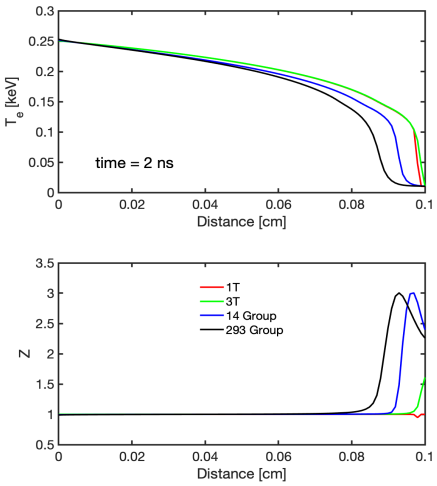

Figure 11: Top: Electron temperature profile across the foam, plotted for each algorithm type and calculated at t = 2 ns. Bottom: Ratio of radiation to electron temperature across foam, calculated at 2 ns.

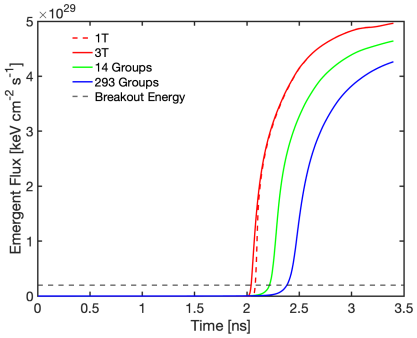

Figure 12: Time resolved emergent flux profile calculated using MDART with each algorithm type described in table 1; 1T (red dashed), 3T (red), 14 groups (green) and 293 groups (blue). The breakout time boundary is shown as the dashed grey line.

The bottom panels of figures 9 - 11 provide an alternative way to view the wave. The parameter z is defined by

$$z = \frac{T_r}{T_e} \tag{39}$$

where we take the radiation energy density to be given by a Planckian distribution at temperature T_r. The radiation temperature is calculated using

$$T_r = \left[\frac{1}{a}\sum_{i\leq N} E_i\right]^{\frac{1}{4}} \tag{40}$$

where N is the number of groups and E_i is the energy density contained within the group i.

6.2.2. *Simulated DANTE flux*

The main diagnostic in modern radiation wave experiment is the emergent flux which is detected using a DANTE detector. Both the breakout time and peak flux measurements can provide insight to to conditions within the material and for the drive profile. The time resolved emergent flux signal is shown in figure 12 for each simulation type. The breakout times associated with each algorithm type are given in table 2.

Simulation Type	Breakout Time [ns]
1T	2.08
3T [29]	2.04
14-Group	2.22
Nominal	2.38

Table 2: Breakout times obtained from each simulation type. Breakout time taken to be point where flux exceeds 2×10^{28} keV cm^{-2} s^{-1}.

6.2.3. *Marshak wave profile*

Figures 9, 10 and 11 show that group number changes the overall shape of the wavefront with lower group numbers resulting in a steeper gradient defining the front, for all timepoints shown. This is explained by the difference in opacity for high and low energy photons when one increases the group number sufficiently to completely distinguish them. Generally, higher energy photons experience a lower opacity and, where group numbers are large enough, this smaller opacity permits a 'preheat' signature that precedes the main front, evident in the nominal and 14 group case. Similarly, low energy photons experience a larger opacity and cannot penetrate so far into the material. These effects cause the front to stretch out spatially with increasing group numbers. This analysis is corroborated by the profile of z at each time-point, which shows how the radiation penetration rate differs as the group number increases. In the 1T case, z remains constant at unity throughout the simulation since $T_r = T_e$. In the 3T case, z is strongly peaked at the position of the wavefront at each time-point. Thus, the radiation field and the material are still strongly coupled in this regime, suggesting the specific heat and Planckian opacity are sufficiently high that any radiation energy locally deposited will be absorbed very quickly by the material. From a spatially and temporally resolved plot of z, an estimate of the photon-electron relaxation time could be obtained by calculating how long it takes for $z \to 1$ at a particular point in space.

For the multigroup cases, z exhibits the same sharp drop off behind the peak but shows a much higher level of preheat, indicated by the regions of $T_r > T_e$ preceding the main peak. The extent of this preheat is dominated by the value of κ_R in each group, with high energy photons penetrating deeper. This increases the radiation temperature but, since the energy has not fully been absorbed by the material due to the lower opacity, the electron temperature will remain relatively unchanged. The solutions tend to the nominal case as group numbers increase. Comparing the 3T and 1T simulations, the latter displays a much sharper shoulder on the wavefront, due to the instantaneous coupling between the material and radiation.

This analysis is further confirmed from the emergent flux signatures shown in figure 12. The lack of preheat in the single group algorithms manifests as a sharply defined breakout time, with an almost vertical rise. The multigroup algorithms have a more modest increase, showing an initial pre breakout signature due to high energy photons penetrating deep into the material. Following this, the signal increases sharply as in the sin-

gle group case. By the end of the simulation, the peak flux is larger for the single group algorithm, but since the drive is only on until 3.5 ns in these simulations a full conclusion to how the peak flux changes with group number cannot be drawn.

6.2.4. Marshak wave speed

For all timepoints considered, the wavefront travels more quickly in low group number cases. The 3T and 14 group algorithms lead the nominal 293 group by 7% and 15%, respectively, calculated from the breakout time measurements in table 2. Such discrepancies are larger than errors associated with physical parameters such as density fluctuations and drive uncertainties [6] [19]

Figure 13 compares the weighted opacities as calculated using a 3T algorithm and a nominal 293 group calculation, at an electron temperature of around 240eV. In the nominal case, the group number is sufficiently large that each weighted opacity gives a good approximation to the frequency resolved profile. When the REE is solved using a 3T algorithm, the weighted opacities used in the calculation are shown as red dashed lines in figure 13. The value of κ_R used in a 3T algorithm is an underestimation of the nominal opacity in regions where a high number of photons are present. This results in the wave travelling faster. This effect will remain until the number of groups is large enough that both weighted opacities tend to the frequency resolved values, which is why the effect is still present in the 14 group cases. Above 2.5 keV, the 3T value of κ_R becomes larger than the nominal value, which prohibits a preheat signature from high energy photons. Similarly, the value of κ_P used in a 3T algorithm is higher than the nominal value in the energy region of high photon number . This over-estimate of κ_P causes a strong coupling between the radiation and electrons, indicated by the sharp form of z in the 3T cases in figures 9 to 11. Although figure 13 shows results for a single temperature, the results are characteristic of all temperatures sampled during the simulation.

The peak value of z also changes with group number. The differences between the 14 group and nominal cases are negligible but, as shown in figures 9, 10 and 11, the nominal case peaks at around 50% more than the single group case. Thus, as group number increases, the corresponding increase in penetration depth coupled with a lower opacity in high energy groups causes T_r and T_e to differ. This is also due to lack of absorption at the front position.

Using more than 293 groups shows no differences when compared to the nominal case, as is shown in figure 14, where a simulation has been run under the same conditions with 1000 groups. Note that the number of groups necessary to converge the solution ultimately depends on the group boundary positioning. We have not attempted to calculate the optimal number of groups for the model experiment used in this analysis, as it is outside the scope of this paper. Instead we wish to provide the reader with an indication of the discrepancies which arise due to very poor group resolution. However, one can consider 293 as an upper bound on the number of groups necessary for solution convergence though it is likely a smaller number would suffice.

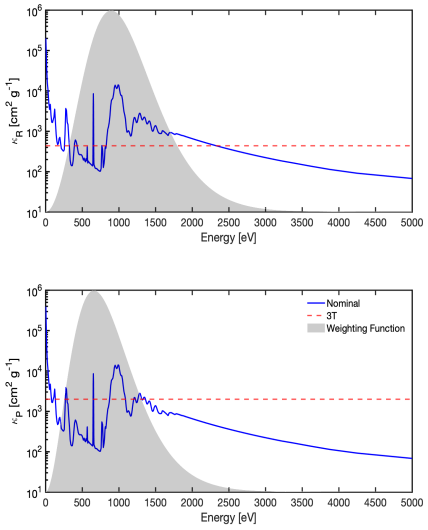

Figure 13: Comparison of Rosseland (top) and Planckian (bottom) weighted opacities as calculated in the nominal (blue lines) and 3T (red dashed line) cases for $T_e = 240eV$. The normalised weighting functions of $\frac{\partial B_\nu(T_e)}{\partial T}$ and $B_\nu(T_e)$ are shown as shaded regions.

7. 3T simulations

As shown from section 6, the breakout time calculated for a Marshak wave is dependant on group number, with increasing group numbers converging to the most accurate value. In the absence of convergence in group number, it is not possible to provide unequivocal evidence that the change in breakout time is solely due to changes in opacity profile. To demonstrate this, we consider changes in incident flux and opacity, modelled using a 3T algorithm, to show that the breakout time results obtained are indistinguishable from the nominal opacity case run using a fully converged algorithm.

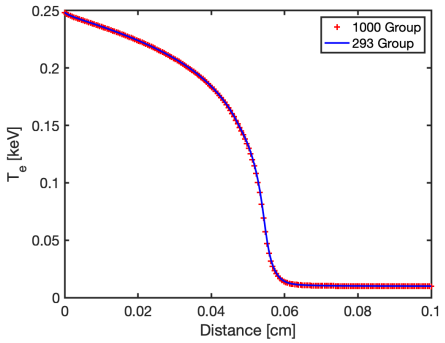

Figure 14: Comparison of Marshak wave progress at $1ns$ as calculated by using 293 (blue line) and 1000 (red cross) groups. This plot demonstrates that 293 groups is sufficiently high definition that the results have converged in group number.

7.1. Percentage change in opacity

Typically, κ_R and κ_P differ considerably in a single group algorithm, as shown in figure 15. Due to the presence of both opacities in the calculations, changing the opacity can be achieved in 2 separate ways; one could alter the frequency resolved opacity to change both κ_R and κ_P, or vary each individually. The second method provides further insight into how the wave propagates, as discussed in the following sections.

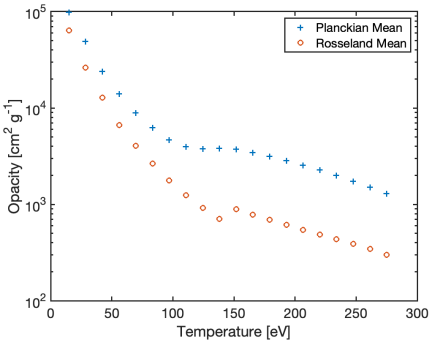

Figure 15: Comparison of Rosseland opacity (κ_R), blue cross, and Planckian opacity (κ_P), red circle as a function of temperature using single group weighted averages, where the average is taken across the entire energy spectrum.

7.2. Changing both opacities

To obtain a result close to the nominal case, the wave speed calculated using a 3T algorithm must be decreased. Generally, a higher opacity causes the wave to propagate slower [39], so the opacity needs to increase to match the nominal case. Figure 16 shows a comparison between the nominal case and a 3T algorithm run with a 30% enhancement to both κ_P and κ_R.

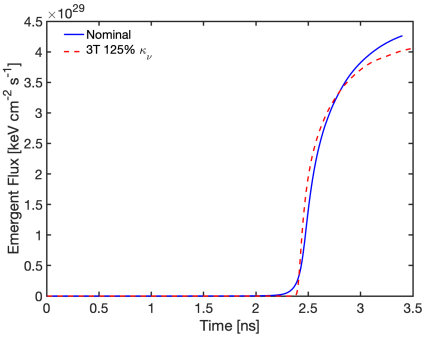

Figure 16: Comparison of nominal 293 group DANTE flux signature with 3T algorithm run with a 25% enhancement on radiative opacity.

Figure 16 shows that using a 3T algorithm, a breakout time of 2.5 ns could be falsely attributed to a higher than expected opacity value, but is actually due to a poor group stencil.

7.3. Changing Rosseland mean only

Figure 17 shows the solution obtained where a 30% enhancement has been applied to κ_R only.

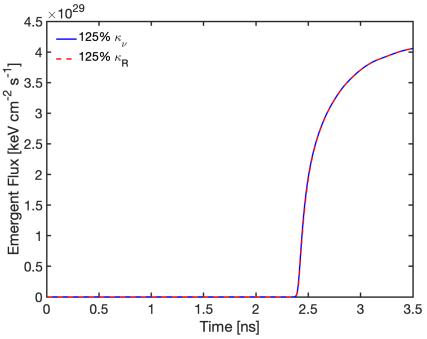

Figure 17: Comparison of time resolved emergent flux generated from a 25% artificial enhancement on the frequency resolved opacity profile with that generated from 25% enhancement on Rosseland mean only.

The results are almost identical whether both opacities or only κ_R is enhanced, demonstrating the importance of κ_R in Marshak wave calculations.

7.4. Changing Planckian mean only

The 30% enhancement is now applied to κ_P and is shown in figure 18. The solution is in good agreement with the 3T solution from figure 12, demonstrating that κ_P is not as important in the system studied. Despite the fact that changing the Planck opacity doesn't appear to have any effect on this situation, κ_P still has an important role in systems generally. The value of β, which

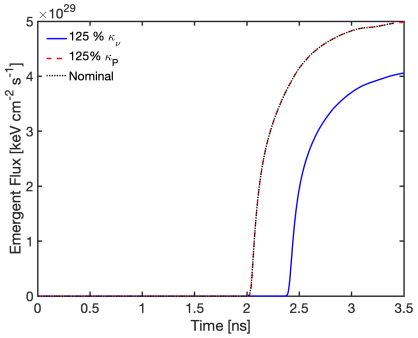

Figure 18: Comparison of time resolved emergent flux generated from a 25% artificial enhancement on the frequency resolved opacity profile with that generated from 25% enhancement on Planckian mean only. The black dotted line corresponds to the 3T case shown in figure 12.

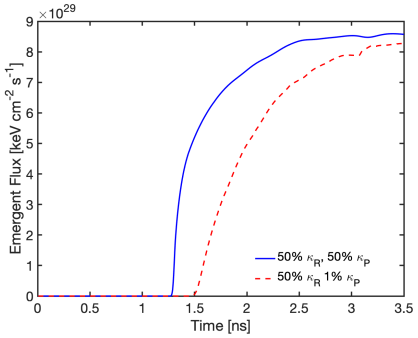

Figure 19: Comparison of time resolved emergent flux generated from a 50% artificial reduction on radiative opacity with that generated from a 50% reduction on κ_R and 99% reduction on κ_P.

is defined in equation 21, describes the strength of coupling between the radiation field and the electron temperature, with higher value of β representing a stronger coupling. An increase in β can result from an increase in κ_P or a *decrease* in c_V. These represent, respectively, an increase in the coupling between the radiation-material energy density and a decrease in the material energy density required to increase the electron temperature. Since both contributions will affect T_e, they are both important.

To demonstrate this point, we reduce the value of κ_P and κ_R to show a situation where the radiation is forced to decouple from the material. This is shown in figure 19, which compares solutions for two sets of scenarios; a 50% decrease in both κ_R and κ_P and an extreme case of 50%κ_R and 1%κ_P. For the latter case, decoupling of radiation and electrons means the radiation wave takes longer to traverse the foam.

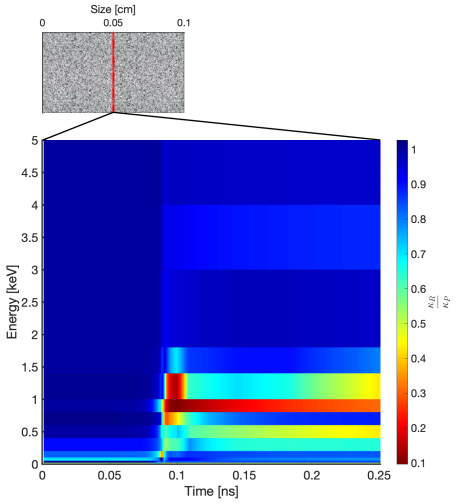

Figure 20: Evolution of $\frac{\kappa_R}{\kappa_P}$ as a function of time and energy, shown for 14 group simulations. The plot shown is calculated at the foam midpoint, shown by the red vertical line bisecting the foam at the top of the figure.

8. Multigroup simulations

Although the results from the simulations discussed in section 7 provide insight to the limitations of 3T algorithms, the problems encountered and analysed are not specific to a 3T framework and are still relevant to under-resolved multigroup schemes. However, in this section we use the multigroup algorithm to test the sensitivity and convergence of other parameters within the scheme.

8.1. Use of single weighted opacity

In section 2, we introduced 3 distinct opacities; the fully resolved opacity, κ_ν, along with the Rosseland and Planckian means, κ_R and κ_P respectively. In a simulation involved a small number of groups, the form of each of these opacities differs significantly, as shown in figure 15. However, if $\kappa_\nu \rightarrow \kappa_R$ in equation 3, then solutions will yield the correct spatial energy transport in the diffusion limit. Conversely, if $\kappa_\nu \rightarrow \kappa_P$, then solutions yield the correct local balance of electron-radiation energy exchange [40]. It is therefore considered an option in multigroup algorithms to use only one of these weighted opacities [12].

Figure 20 shows the variation of $\frac{\kappa_R}{\kappa_P}$ as a function of time and energy where data is taken from the midpoint of the foam, located at $x = 0.05cm$. The difference between both opacities is clearly evident and, near the wavefront, can be an order of magnitude.

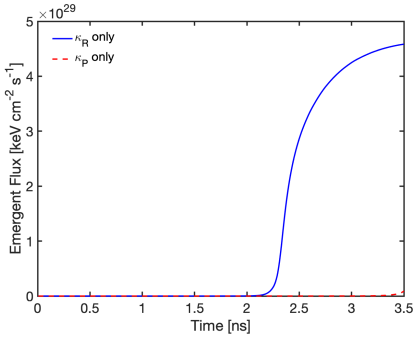

Figure 21: Time resolved emergent flux profile calculated using only κ_R (block) or only κ_P (dashed) for the case of 14 groups. Note that the κ_P profile lies along the x-axis until around 3.4ns.

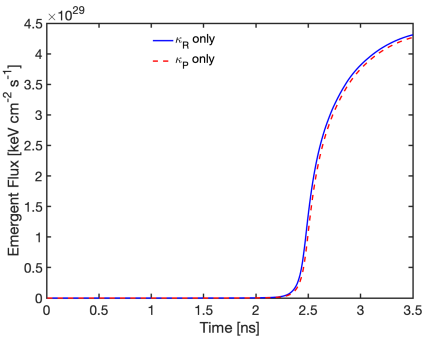

Figure 22: Time resolved emergent flux profile calculated using only κ_R (block) or only κ_P (dashed) for the case of 293 groups.

Figure 21 compares the two different solutions obtained when one uses only either κ_P or κ_R in solving the REE. Using κ_R leads to an increase in wave speed, since the reciprocal form of this opacity enhances optically thin regions of the spectrum. A higher number of groups reduce this effect, as shown in figure 22, where 293 group are used. Finally, the same approach is used in a 3T algorithm which demonstrates that use of κ_P results in a much slower wave profile, use of κ_P in any single group algorithm has the potential to lead to catastrophically inaccurate results. This could have implications for gray discrete ordinate and IMC methods, where no real separation of κ_R and κ_P is defined.

8.2. *Flux limiter changes*

In any FLD algorithm, the choice of flux limiter may effect the final result. This is the case for the current study; for all figures shown so far, the Wilson max flux limiter has been used. Figure 24 shows the change in emergent flux profile where a Wilson Max, Wilson Sum and Larsen n = 2 flux limiter is used.

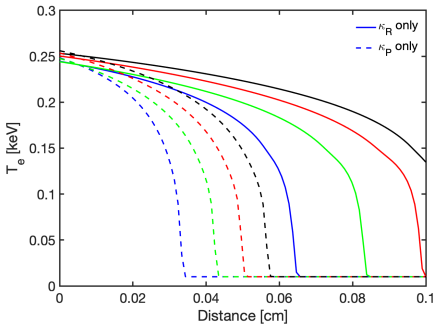

Figure 23: Time resolved emergent flux profile calculated using only κ_R (block) or only κ_P (dashed) for the 3T case.

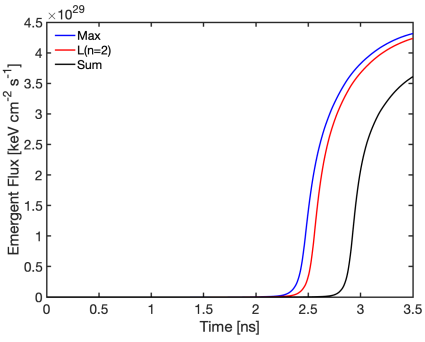

Figure 24: Emergent flux profiles obtained using three different types of flux limiter; Wilson Max (blue), Larsen (n = 2) (red) and Wilson sum (black).

As shown, the choice of flux limiter does change the breakout time obtained from the algorithm, with the different between Max and Larsen n = 2 flux limiter around 3.6%. The sum flux limiter results in a much larger breakout time, this is expected as it uses a simple linear function to relate the free streaming and flux limited regimes of transport which becomes inaccurate under the experimental conditions. Importantly, regardless of the flux limiter type used in the simulation, the discrepancies associated with the group number and opacity details discussed in the previous sections will still be important to the analysis. Nevertheless, one of the flux limiters will provide the most accurate solution to the real transport solution.

9. Discussion

The results presented in this work highlight the necessary caution which must be taken when modelling radiation wave experiments using 3T or multigroup algorithms. We have demonstrated that an under-resolved group structure leads to results which are inaccurate. For the opacity profiles of iron oxide, we have shown that comparisons between using a 1D single group 3T and a 14 group multigroup diffusion algorithm show that the Marshak wave breakout time drops by around 7%. A discrepancy of 14% arises when one compares a 3T algorithm with the fully resolved multigroup solution. These types of errors are comparable with experimental errors [19] [3] [6] and could change the outcome of experimental analysis, particularly where changes in wave breakout time are used as a diagnostic, which in the case of the experiment outline in section 5. We have further shown that changes in the Marshak wave breakout time cannot be attributed solely to changes in physical parameters unless convergence checks in group number have been carried out. In addition to this, we have provided a multigroup analysis of how each respective weighted opacity affects the energy transport through material, applying artificial changes to both the Rosseland and Planckian opacities and monitoring how the wave profile changes. The difference in outcomes by using only κ_R or κ_P in the numerical scheme has also been considered - showing that the weighting of any opacity tends to becomes less important as the group number increases, but is very important in the 3T regime. Finally, we have shown that the role of the flux limiter is important, as expected, and should be considered carefully in this type of analysis. Importantly, although there is a non-negligible deviation between exact transport behaviour and FLD [17] the sensitivity to group structure remains similar, regardless the specific choice of the flux limiter. Thus, results shown in this study are important for any FLD modelling of radiation wave experiments.

9.1. Limitations

As explained in the introduction, this study is not intended to provide the most accurate or detailed account of radiation wave experiments. Rather, under the assumption that the transport is diffusive, we seek to provide a detailed analysis of computational artefacts which could jeopardise analysis where flux limited diffusion is used. A direct comparison between FLD and IMC is not available for the experiment used as a model for the analysis as the data was not obtainable. Nevertheless, as previously stated, the flux limiter study demonstrates that the discrepancies discussed in this paper remain, regardless of flux limiter type.

The algorithm used is 1D and therefore doesn't include any energy losses due to 2D effects, which have been shown to cause notable changes in Marshak speed [1]. The three main 2D effects in radiation wave experiments are

- Energy loss to the gold which surrounds the curved surface of the foam
- Slowing of the wave near the wall surfaces as ablation increases the foam density, and thus its opacity
- Change of cross sectional area reducing the effective flux which enters the foam.

The latter is the least important to the modelling [1] and, for the experiment used as a surrogate model in this work, the aspect ratio is such that the Marshak wave curvature does not effect the wave breakout time across most of the wavefront [41]. To model the energy loss from heating the gold walls, the '1.5D' formula from [1] is used. This approach uses the exact self-similar solution of the diffusive solution [42], which is exact for the opaque gold coating. The resultant energy loss is used to calculate a corresponding reduction on the drive flux flowing into the system. The effect of the wall loss mechanism on emergent flux is demonstrated in figure 25, which shows the results for a 3T, 14-group and 293-group algorithm.

The inclusion of wall loss in the calculation increases the breakout time and lowers the maximum flux detected, as one would intuitively expect. However, the changes are consistent across all group numbers which suggest that the errors explored in earlier chapters will

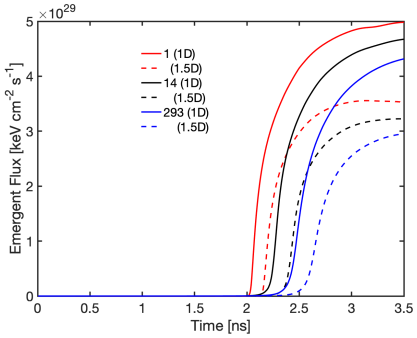

Figure 25: Time resolved emergent flux profiles calculated with (dashed) and without (block) energy loss to gold walls. The numbers in the legend correspond to the number of groups used in the algorithm run.

be present and influential even if 2D effects are included. Additionally, the time discrepancy introduced when 2D effects are accounted for is not consistent across changing group numbers - higher group resolution results in a larger change in breakout time when 1D and 2D cases are compared. This is because higher group numbers allow the high energy preheating photons to be accounted for more accurately. These photons penetrate deep into the material and, as a result, reach more points on the gold cylinder, leading to an increase in energy loss and a slowing of the wave. This again demonstrates the important of fidelity in energy space; higher group numbers are necessary to more accurately account for 2D effects.

Acknowledgements

This work was supported by AWE Aldermaston. The authors are grateful for the comments and suggested improvements from the anonymous referees.

[1] A. P. Cohen, G. Malamud, and S. I. Heizler, "Key to understanding supersonic radiative Marshak waves using simple models and advanced simulations," *Physical Review Research*, vol. 2, no. 2, p. 23007, 2020.

[2] C. A. Back, J. D. Bauer, J. H. Hammer, B. F. Lasinski, R. E. Turner, P. W. Rambo, O. L. Landen, L. J. Suter, M. D. Rosen, and W. W. Hsing, "Diffusive, supersonic x-ray transport in radiatively heated foam cylinders," *Physics of Plasmas*, vol. 7, no. 5, pp. 2126–2134, 2000.

[3] A. S. Moore, T. M. Guymer, J. Morton, B. Williams, J. L. Kline, N. Bazin, C. Bentley, S. Allan, K. Brent, A. J. Comley, K. Flippo, J. Cowan, J. M. Taccetti, K. Mussack-Tamashiro, D. W. Schmidt, C. E. Hamilton, K. Obrey, N. E. Lanier, J. B. Workman, and R. M. Stevenson, "Characterization of supersonic radiation diffusion waves," *Journal of Quantitative Spectroscopy and Radiative Transfer*, vol. 159, pp. 19–28, 2015.

[4] C. A. Back, J. D. Bauer, O. L. Landen, R. E. Turner, B. F. Lasinski, J. H. Hammer, M. D. Rosen, L. J. Suter, and W. H. Hsing, "Detailed measurements of a diffusive supersonic wave in a radiatively heated foam," *Physical Review Letters*, vol. 84, no. 2, pp. 274–277, 2000.

[5] J. Massen, G. D. Tsakiris, K. Eidmann, I. B. Földes, T. Löwer, R. Sigel, S. Witkowski, H. Nishimura, T. Endo, H. Shiraga, M. Takagi, Y. Kato, and S. Nakai, "Supersonic radiative heat waves in low-density high-Z material," *Physical Review E*, 1994.

[6] D. J. Hoarty, J. Morton, M. Jeffery, L. K. Pattison, A. Wardlow, S. P. D. Mangles, S. J. Rose, C. Iglesias, K. Opachich, R. F. Heeter, and T. S. Perry, "High Energy Density Physics A proposal to measure iron opacity at conditions close to the solar convective zone-radiative zone boundary," *High Energy Density Physics*, vol. 32, no. May, pp. 70–76, 2019.

[7] J. A. Fleck and J. D. Cummings, "An implicit Monte Carlo scheme for calculating time and frequency dependent nonlinear radiation transport," *Journal of Computational Physics*, vol. 8, no. 3, pp. 313–342, 1971.

[8] S. I. Blinnikov, R. Eastman, O. S. Bartunov, V. A. Popolitov, and S. E. Woosley, "A Comparative Modeling of Supernova 1993J," *The Astrophysical Journal*, vol. 496, no. 1, pp. 454–472, 1998.

[9] D. S. Clark, A. L. Kritcher, J. L. Milovich, J. D. Salmonson, C. R. Weber, S. W. Haan, B. A. Hammel, D. E. Hinkel, M. M. Marinak, M. V. Patel, and S. M. Sepke, "Capsule modeling of high foot implosion experiments on the National Ignition Facility," *Plasma Physics and Controlled Fusion*, vol. 59, no. 5, 2017.

[10] M. Klassen, R. Kuiper, R. E. Pudritz, T. Peters, R. Banerjee, and L. Buntemeyer, "A general hybrid radiation transport scheme for star formation simulations on an adaptive grid," *Astrophysical Journal*, vol. 797, no. 1, 2014.

[11] M. M. Marinak, G. D. Kerbel, N. A. Gentile, O. Jones, D. Munro, S. Pollaine, T. R. Dittrich, and S. W. Haan, "Three-dimensional HYDRA simulations of National Ignition Facility targets," *Physics of Plasmas*, vol. 8, no. 5 II, pp. 2275–2280, 2001.

[12] E. S. Myra and W. D. Hawkins, "A comparison study of discrete-ordinates and flux-limited diffusion methods for modeling radiation transport," *High Energy Density Physics*, vol. 9, no. 1, pp. 91–102, 2013.

[13] C. Orban, M. Fatenejad, S. Chawla, S. C. Wilks, and D. Q. Lamb, "A Radiation-Hydrodynamics Code Comparison for Laser-Produced Plasmas: FLASH versus HYDRA and the Results of Validation Experiments," vol. 2, no. 1, pp. 1–21, 2013.

[14] P. B. Radha, V. N. Goncharov, T. J. Collins, J. A. Delettrez, Y. Elbaz, V. Y. Glebov, R. L. Keck, D. E. Keller, J. P. Knauer, J. A. Marozas, F. J. Marshall, P. W. McKenty, D. D. Meyerhofer, S. P. Regan, T. C. Sangster, D. Shvarts, S. Skupsky, Y. Srebro, R. P. Town, and C. Stoeckl, "Two-dimensional simulations of plastic-shell, direct-drive implosions on OMEGA," *Physics of Plasmas*, vol. 12, no. 3, pp. 1–18, 2005.

[15] M. Rosen, "The physics of radiation driven ICF hohlraums," 1995.

[16] A. I. Shestakov and S. S. Offner, "A multigroup diffusion solver using pseudo transient continuation for a radiation-hydrodynamic code with patch-based AMR," *Journal of Computational Physics*, vol. 227, no. 3, pp. 2154–2186, 2008.

[17] A. P. Cohen and S. I. Heizler, "Multi-group discontinuous asymptotic P1 approximation in radiative Marshak waves experiments," *Journal of Quantitative Spectroscopy and Radiative Transfer*, vol. 272, p. 107822, 2021.

[18] J. E. Bailey, T. Nagayama, G. P. Loisel, G. A. Rochau, C. Blancard, J. Colgan, P. Cosse, G. Faussurier, C. J. Fontes, F. Gilleron, I. Golovkin, S. B. Hansen, C. A. Iglesias, D. P. Kilcrease, J. J. Macfarlane, R. C. Mancini, S. N. Nahar, C. Orban, J. Pain,

A. K. Pradhan, M. Sherrill, and B. G. Wilson, "A higher-than-predicted measurement of iron opacity at solar interior temperatures," *Nature*, vol. 517, pp. 56–59, 2015.
[19] C. L. Fryer, E. Dodd, W. Even, C. J. Fontes, C. Greeff, A. Hungerford, J. Kline, K. Mussack, I. Tregillis, J. B. Workman, J. Benstead, T. M. Guymer, A. S. Moore, and J. Morton, "Uncertainties in radiation flow experiments," *High Energy Density Physics*, vol. 18, pp. 45–54, 2016.
[20] G. B. Rybicki and A. P. Lightman, *Radiative Processes in Astrophysics*. 1985.
[21] J. I. Castor, *Radiation hydrodynamics*. Cambridge University Press, 2006.
[22] G. B. Rybicki and A. P. Lightman, *Radiative processes in astrophysics*. New York, 1979.
[23] G. C. Pomraning, *The Equations of Radiation Hydrodynamics, by G.C. Pomraning*. Pergamon Press, 1973.
[24] A. Fick, " V. On liquid diffusion ," *The London, Edinburgh, and Dublin Philosophical Magazine and Journal of Science*, vol. 10, no. 63, pp. 30–39, 1855.
[25] C. D. Levermore and G. C. Pomraning, "A flux-limited diffusion theory," *The Astrophysical Journal*, 1981.
[26] W. F. Huebner and W. D. Barfield, *Opacity*. Springer, 2014.
[27] G. L. Olson, L. H. Auer, and M. L. Hall, "Diffusion, P1 , and other approximate forms of radiation transport," *Journal of Quantitative Spectroscopy and Radiative Transfer*, vol. 64, no. 6, pp. 619–634, 1999.
[28] G. C. Pomraning, "A Comparison of Various Flux Limiters and Eddington Factors," tech. rep., University of California Livermore, 1981.
[29] G. S. Fraley, E. J. Linnebur, R. J. Mason, and R. L. Morse, "Thermonuclear burn characteristics of compressed deuterium-tritium microspheres," *Physics of Fluids*, 1974.
[30] K. McLean and S. Rose, "Corrections to weighted opacities and energy exchange rate in 3-T radiation-hydrodynamics," *High Energy Density Physics*, vol. 35, no. November 2019, p. 100734, 2020.
[31] F. Graziani, "Radiation diffusion: An overview of physical and numerical concepts," pp. 29–66.
[32] W. H. Press, *Numerical recipes in FORTRAN*. Cambridge Univ. Pr., 1994.
[33] W. D. Barfield, "A comparison of diffusion theory and transport theory results for the penetration of radiation into plane semiinfinite slabs," *Los Alamos Scientific Laboratory of the University of California, Technical Report*, 1954.
[34] B. Su and G. L. Olson, "Benchmark Results for the Non-Equilibrium Marshak Diffusion Problem," *Journal of Quantitative Spectroscopy and Radiative Transfer*, vol. 56, no. 3, pp. 337–351, 1996.
[35] G. C. Pomraning, "The non-equilibrium Marshak wave problem," *Journal of Quantitative Spectroscopy and Radiative Transfer*, vol. 21, no. 3, pp. 249–261, 1979.
[36] S. Basu and H. M. Antia, "Helioseismology and solar abundances," *Physics Reports*, vol. 457, no. 5-6, pp. 217–283, 2008.
[37] S. J. Rose, "Calculations of the radiative opacity of laser-produced plasmas," *Journal of Physics B: Atomic, Molecular and Optical Physics*, vol. 25, no. December 1991, pp. 1667–1681, 1992.
[38] M. F. Kasim, T. P. Galligan, J. Topp-Mugglestone, G. Gregori, and S. M. Vinko, "Inverse problem instabilities in large-scale modeling of matter in extreme conditions," *Physics of Plasmas*, vol. 26, no. 11, 2019.
[39] R. E. Marshak, "Effect of radiation on shock wave behavior," *Physics of Fluids*, vol. 1, no. 1, pp. 24–29, 1958.
[40] D. Mihalas and B. W. Mihalas, *Foundations of radiation hydrodynamics*. Dover Publications, INC, 2018.
[41] D. J. Hoarty, "Private Communication," 2021.
[42] T. Shussman and S. I. Heizler, "Full self-similar solutions of the subsonic radiative heat equations," *Physics of Plasmas*, vol. 22, no. 8, pp. 1–13, 2015.